+Electronic Supplementary Information for

Halogen-Bond Chemistry-Rectified Hypervalent Tellurium Redox Kinetics towards High-Energy Zn Batteries

Jintu Qi,[a] Yongchao Tang,*[ab] Yue Wei,[c] Guigui Liu,[a] Jianping Yan,[a] Zhenfeng Feng,[a] Zixin Han,[a] Minghui Ye,[a] Wencheng Du,[bd] Qi Yang,[e] Yufei Zhang,[ab] Zhipeng Wen,[ab] Xiaoqing Liu,[ab] and Cheng Chao Li*[ab]

[a] School of Chemical Engineering and Light Industry, Guangdong University of Technology, Guangzhou, 510006, People's Republic of China.

[b] Guangdong Provincial Laboratory of Chemistry and Fine Chemical Engineering Jieyang Center, Jieyang, 515200, P. R. China.

[c] School of Environment and Civil Engineering, Dongguan University of Technology, Dongguan, Guangdong 523808, P. R. China.

[d] School of Advanced Manufacturing, Guangdong University of Technology, Jieyang 522000, People's Republic of China.

[e] State Key Laboratory of Chemical Resource Engineering, College of Chemical Engineering, Beijing University of Chemical Technology, Beijing 100029, P. R. China.

Email: tyc@gdut.edu.cn, licc@gdut.edu.cn

1. Experimental Section

1.1 Material Synthesis

The mesoporous carbon encapsulated Te (Te@CMK-3) was prepared based on the previous method.[1] CMK-3 (99.9%, JCNANO) and fresh Te powder (99.99%, Aladdin) with a 1:2 weight ratio was mixed through wet ball-milling in isopropanol at 400 r/min for 10 h. After evaporating isopropanol in the air at 60 °C, the mixture was pressed into a pellet at 10 MPa and then calcined at 600 °C for 10 h in a sealed quartz tube filled with Ar to get the Te@CMK-3 composite.

1.2 Electrolyte Preparation

1-butyl-3-vinylimidazolium cation ($VBIM^+$) with a large cation radius and low symmetry is chosen for electrolyte preparation to achieve a low melting point.[2-4] The VB-Br/F ILE was prepared by mixing $ZnBr_2$ (99.9%, Aladdin), 1-butyl-3-vinylimidazolium bromide (VBIMBr, 98%, Macklin), and ZnF_2 (99.9%, Aladdin) with a molar ratio of 1:1.2:0.05. Subsequently, the mixture was stirred at 110 °C for 8 h, ensuring a complete Lewis acid-base reaction. Finally, the VB-Br/F ILE was maintained at room temperature for 6 h before use. Furthermore, 0.35 M of dichloroethane (DCE, 99.5%, Macklin) was added into the resultant VB-Br/F to obtain VB-Br/F-DCE. Similarly, VB-Br/F-CAN was also prepared by adding 0.35 M of chloroacetonitrile (CAN, 99%, J&K Scientific) into VB-Br/F. The VB-Cl/F and VB-Cl/F-DCE were prepared by a similar method to that for VB-Br/F and VB-Br/F-DCE, but using $ZnCl_2$ (99.9%, Macklin) to replace the $ZnBr_2$ (99.9%, Aladdin). It is noted that the electrolyte was prepared in a glovebox filled with argon atmosphere.

1.3 Materials characterization

The synthesized Te@CMK-3 composite was characterized by X-ray diffraction (XRD, Rigaku SmartLab, CuKα radiation, λ = 1.5406 Å), scanning electron microscopy (SEM, Hitachi SU8220 after freeze-dried), thermogravimetric analysis (TGA, TG/DTA 6300). Transmission electron microscopy (TEM, JEOL-JEM2100F) and high-angle annular dark field transmission electron microscopy (HAADF-STEM) were applied to reveal the detailed lattice structure and element distribution with an acceleration voltage of 200 kV. Electrolytes were characterized by a Raman spectrometer (Thermo Scientific DXRXI system with excitation from an Ar laser at 633 nm). The electrolyte viscosity was measured in a dry room environment utilizing an Anton-Paar MCR 102 rheometer, applying a constant shear rate of 10 s^{-1}, and using a Peltier system for temperature control. The viscosity values averaged over 5 min (150 data points) were used. The ionic conductivity was tested by an ionic conductivity meter (CM-25R, TOA-DKK). Differential scanning calorimetry (DSC) was carried out in NETZSCH DSC 200 F. The samples were sealed in a Platinum crucible in a glove box and tested at the temperature of -80~30 °C with a

cooling/heating rate of 5 °C min^{-1}. The samples for NMR measurements were prepared in a dry room. The solution was transferred to NMR tubes with a sealed capillary containing deuterium DMSO as lock and chemical shift reference, and immediately sealed. ^{1}H NMR spectra were carried out with a Bruker Avance 400 MHz NMR. X-ray diffraction (XRD) experiments were performed on the Rigaku SmartLab, CuKα radiation, (λ = 1.5406 Å) system at a range of 2θ = 15-60° (10° min^{-1}). To perform XRD characterization of Te@CMK-3 electrodes, the Zn‖Te batteries using VB-Br/F after charge/discharge tests were disassembled (using a nonconductive plier and tweezer to avoid short-circuit). The disassembled electrodes were sealed in a glass bottle and sent for XRD characterization. Time-of-flight secondary ion mass spectrometry (TOF-IMS) surface analysis was carried out with a TOF secondary ion mass spectrometer (ION-TOF TOF.SIMS5) equipped with a bismuth primary-ion source.

1.4 Electrochemical Measurements

The Te@CMK-3 sample was mixed with Super P and polyvinylidene fluoride in a weight ratio of 8:1:1 in 1-methyl-2-pyrrolidinone (99.9%, Aladdin), and then the slurry was pasted on 600 mesh titanium mesh and dried under vacuum at 80 °C for 12 h. The typical mass loading of active materials is calculated as ~1.2 mg cm^{-2}. Two electrode Swagelok® type cells were assembled with Te cathode, Zn anode, and glass fiber membrane (Whatman) separators, VB-Br/F, VB-Br/F-DCE, VB-Cl/F, and VB-Cl/F-DCE as the electrolyte, respectively. The cell body was composed of Teflon and platinum rod current collectors. The area of separators, Te cathode, and Zn anode was 1.13 cm^{-2}. The thickness of the separator was 0.12 mm. The amount of electrolyte used in a single cell needs to infiltrate the separator (~100 μL). The GCD test was performed on a Neware electrochemical testing system (CT-4008-10V 50mA-164, Shenzhen, China). The energy efficiency was calculated based on the energy ratio of discharge to charge curves, and all these data can be collected by the battery testing system. To calculate the energy efficiencies of Zn||Te batteries in different electrolytes, the batteries were preactivated over 5 cycles at a current density of 0.2 A g^{-1}, and then the average energy efficiencies were calculated based on the GCD curves with a deviation less than 5%. The cyclic voltammetry (CV) and linear scan voltammetry (LSV) test was carried out on a Gamry multi-channel electrochemical workstation, the voltage range is consistent with the cut-off voltage of GCD tests. Electrochemical impedance spectroscopy (EIS) tests were conducted by using the electrochemical workstation (Interface 1010B, Gamry). All tests were conducted at room temperature, and the variable temperature EIS test was performed at 30~70 °C.

1.5 Calculation of the activation energy

The activation energy can be studied by the Arrhenius equation:

$$\frac{1}{R_{ct}} = Aexp\ (-\frac{E_a}{RT})$$

Where R_{ct} is the interfacial resistance, A is the frequency factor, R is the gas constant, and T is the absolute temperature.[5]

2. Theoretical computation section

2.1 MD simulations

All calculations were implemented in Materials Studio with the DMol^3 code. The Perdew–Burke–Ernzerhof (PBE) functional of the generalized gradient approximation (GGA) was used to calculate the exchange-correlation energy. The double numerical plus polarization (DNP) was chosen during the geometry optimization. The DFT-D method of Grimme was employed to describe the van der Waals interactions. The convergence tolerances of energy change, maximum force, and maximum displacement were set as 2×10^{-5} Ha, 0.002 Ha Å^{-1}, and 0.005 Å, respectively. Molecular dynamics (MD) simulations were performed using the Materials Studio Forcite modules. Molecules and ions including DCE, $VBIm^+$, and $ZnBr_4^{2-}$ were built and got geometry optimization through Dmol^3 software. The system was built by an Amorphous Cell module: 35 DCE, 100 $VBIm^+$, and 50 $ZnBr_4^{2-}$. A universal force field was adopted for all molecules and ions. NPT ensemble was used to pre-equilibrate the systems at 298 K for 100 ps, and then NVT ensemble was used to achieve a final equilibrate state of the systems at 298 K for 1 ns. The final 500 ps in NVT production steps were sampled for radial distribution function (RDF) analyses.[6]

2.2 Free energy calculation by DFT

The geometry optimization and density functional theory (DFT) chemical description for the molecular structures of DOPO-PEPA and its derivatives after bond breaking was performed using the Gaussian09 program package with M062X exchange-correlation functional and 6-31G** basis set.[7, 8]

2.3 Equilibrium potential calculation

The change in the Gibbs free energy (ΔG) can be calculated by using the electron-transfer numbers (n) and the difference in the electrochemical potential (ΔU).

$$\Delta G = -neU$$

where n is the electron transfer number, e is the elemental charge, and ΔU is the electrochemical potential difference.[9]

2.4 Chemical bond energy calculation

The bond dissociation energy (BDE) Zn-Br or Zn-Cl of $ZnBr_4^{2-}$ or $ZnCl_4^{2-}$ and the bond formation energy (BFE) of Te-Br or Te-Cl of $TeBr_3^+$ or $TeCl_3^+$ was computed by use of M062X/def2-TZVP level.[10, 11] The BDE was calculated using the following equation:

$$A\text{-}B \rightarrow A\cdot + B\cdot$$

$$BDE = \Delta_f H_T(A\cdot) + \Delta_f H_T(B\cdot) - \Delta_f H_T(AB)$$

Where $\Delta_f H_T(A\cdot)$, $\Delta_f H_T(B\cdot)$ and $\Delta_f H_T(AB)$ correspond to enthalpies of $ZnBr_4^{2-}$ or $ZnCl_4^{2-}$ and its derivatives after bond breaking at 298.15 K, respectively.

In addition, the BFE was computed using the following equation:

$$C\cdot + D\cdot \rightarrow C\text{-}D$$

$$BFE = \Delta_f H_T(CD) - [\Delta_f H_T(C\cdot) + \Delta_f H_T(D\cdot)]$$

Where $\Delta_f H_T(C\cdot)$, $\Delta_f H_T(D\cdot)$ and $\Delta_f H_T(CD)$ correspond to enthalpies of $TeBr_3^+$ or $TeCl_3^+$ and its derivatives after bond breaking at 298.15 K, respectively.[12]

3. Supplementary Figures

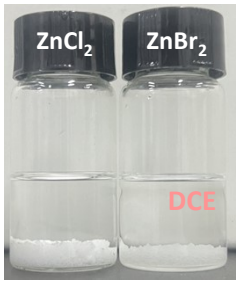

Fig. S1. Optical photographs of 0.3 m $ZnCl_2$ and $ZnBr_2$ in DCE cosolvent.

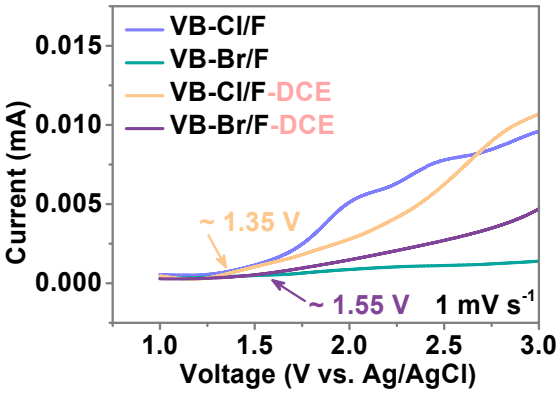

Fig. S2. The LSV curves at a scan rate of 1 mV s^{-1} in different ILEs.

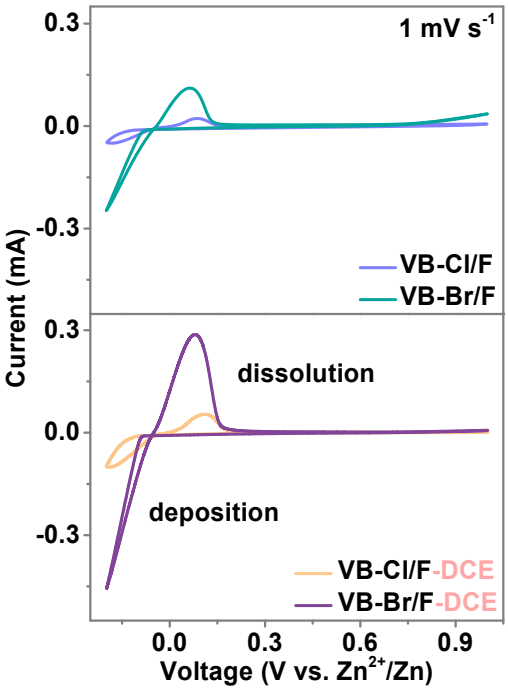

Fig. S3. CV curves of Zn||Ti batteries in different ILEs at a scan rate of 1 mV s^{-1}.

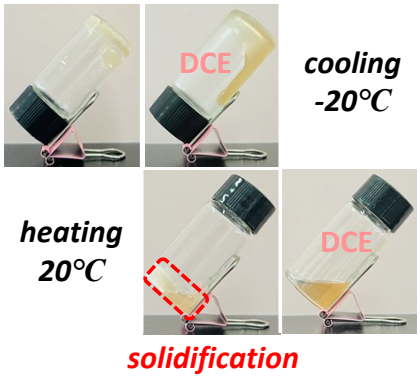

Fig. S4. Optical photographs of VB-Br/F and VB-Br/F-DCE at -20 °C during cooling and 20 °C during reheating. All the ILEs were prepared in a rigidly anhydrous environment.

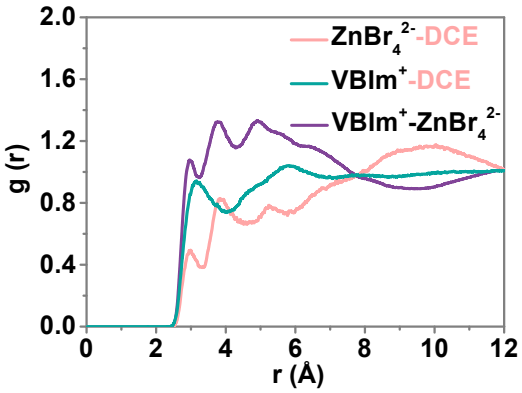

Fig. S5. RDFs of $VBIm^{+}$-$ZnBr_4^{2-}$, DEC-$ZnBr_4^{2-}$, and DEC-$VBIm^{+}$ pairs.

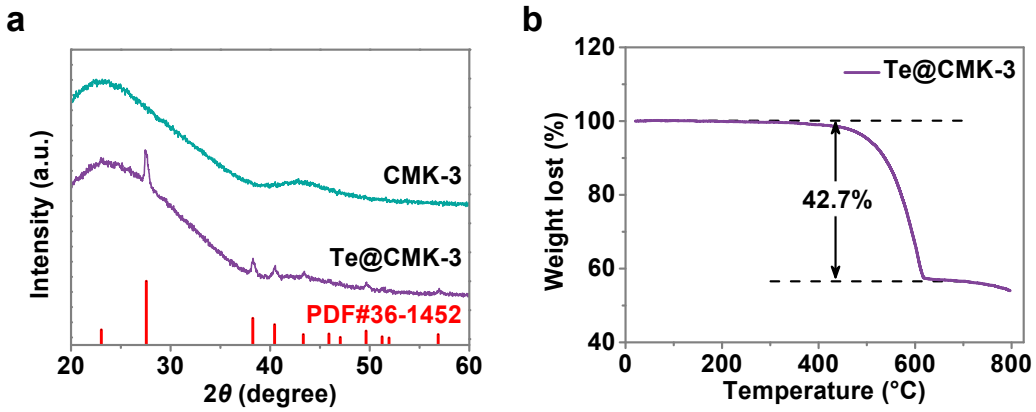

Fig. S6. Chemical composition characterization of the Te@CMK-3: (a) XRD patterns of CMK-3 and Te@CMK-3. (b) TGA curves of Te@CMK-3.

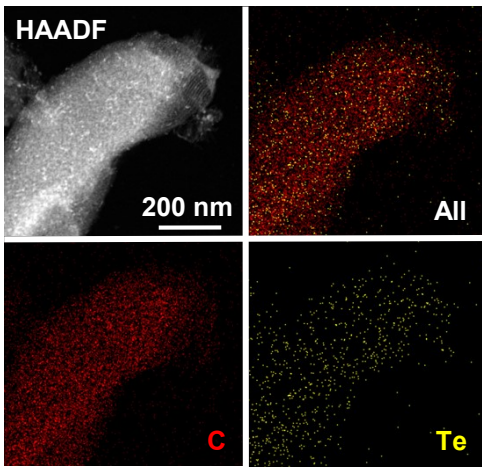

Fig. S7. HAADF image of Te@CMK-3 and corresponding EDS elemental mapping, including Te and C elements.

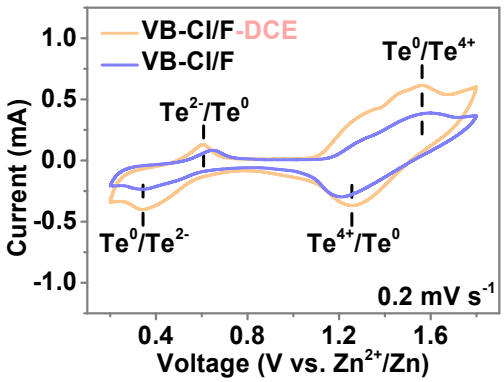

Fig. S8. CV curves of Zn||Te batteries with VB-Cl/F and VB-Cl/F-DCE at a scan rate of 0.2 mV s^{-1}.

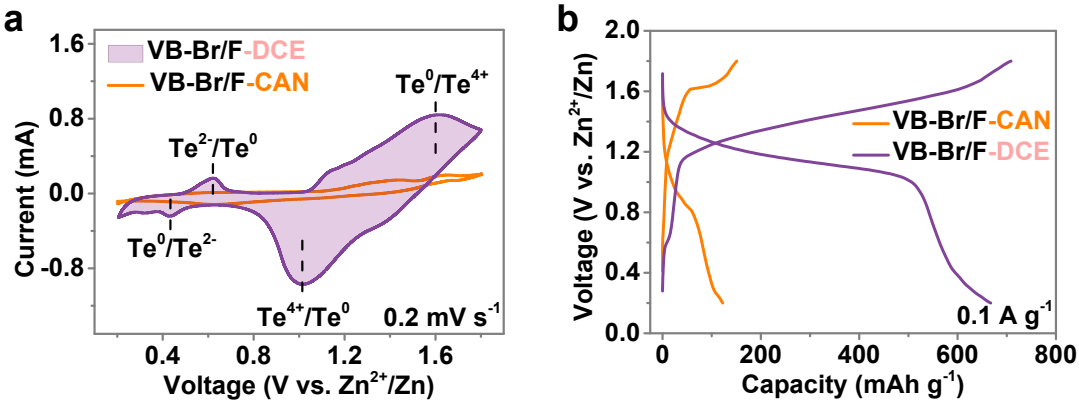

Fig. S9. (a) CV curves of Zn||Te batteries with VB-Br/F-DCE and VB-Br/F-CAN at a scan rate of 0.2 mV s^{-1}. (b) GCD curves of Zn||Te batteries with VB-Br/F-DCE and VB-Br/F-CAN at a current density of 0.1 A g^{-1}.

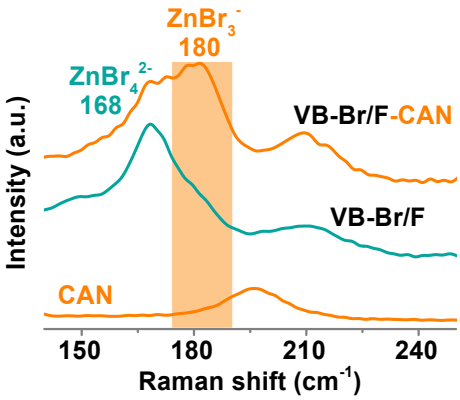

Fig. S10. Raman spectra of CAN, VB-Br/F, and VB-Br/F-CAN electrolytes.

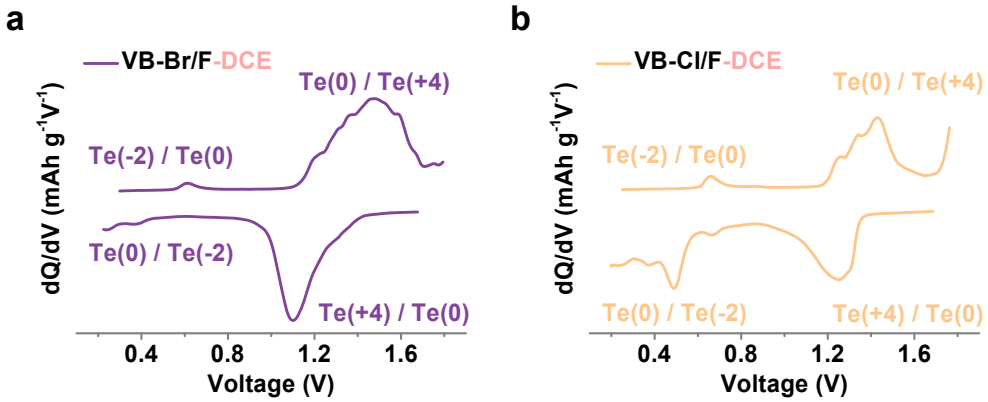

Fig. S11. dQ/dV curves of Zn||Te batteries in (a) VB-Br/F-DCE and (b) VB-Cl/F-DCE.

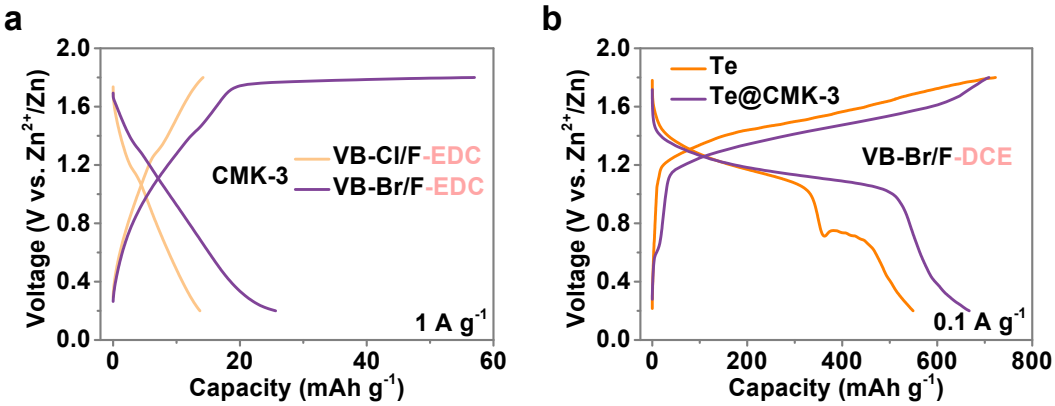

Fig. S12. (a) GCD curves of the Zn||CMK-3 battery in VB-Br/F-DCE and VB-Cl/F-DCE. (b) GCD curves of the Zn||Te battery in VB-Br/F-DCE.

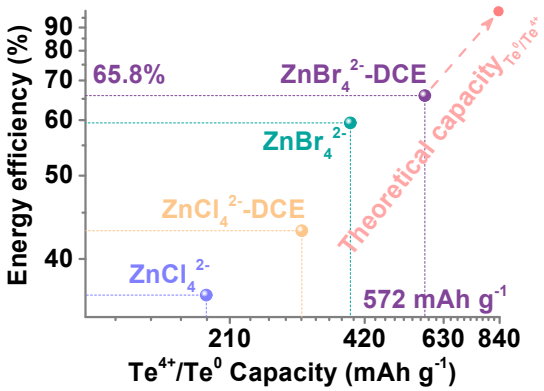

Fig. S13. Energy efficiency comparison of positive-valence Te conversion in Zn||Te batteries with different nucleophilic active metal complex anions.

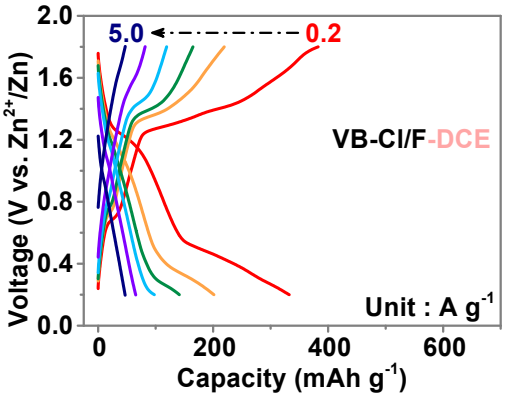

Fig. S14. GCD profiles of Zn||Te battery in VB-Cl/F-DCE at different current densities corresponding to the rate capability in Figure 4a.

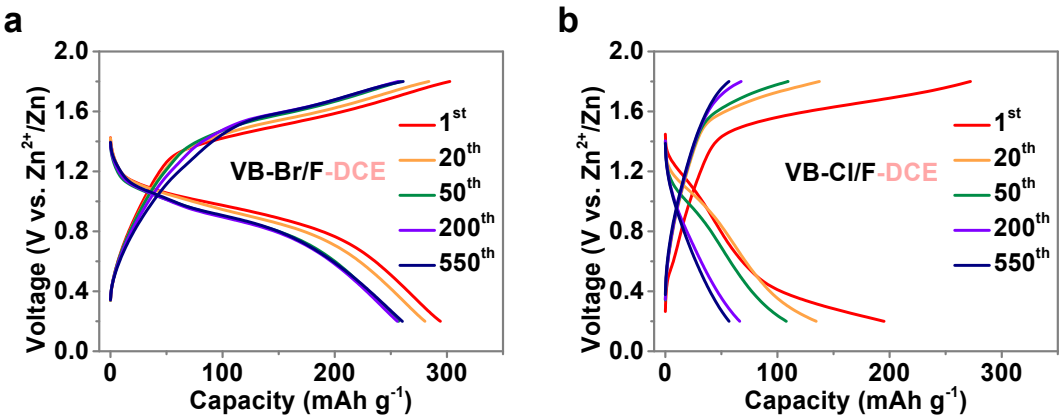

Fig. S15. GCD profiles of Zn‖Te batteries at a current density of 1 A g^{-1} in: (a) VB-Br/F-DCE and (b) VB-Cl/F-DCE.

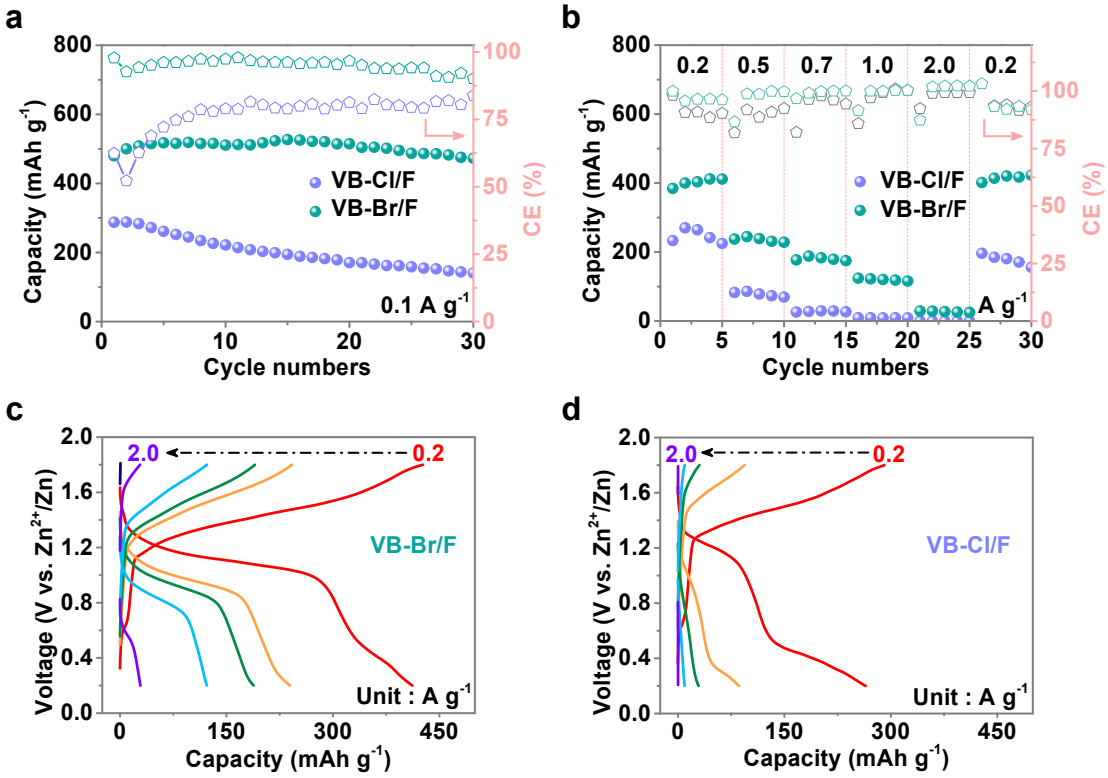

Fig. S16. Electrochemical performance of Zn||Te batteries in VB-Br/F and VB-Cl/F: (a) Discharge capacity and CE at a current density of 0.1 A g^{-1}. (b) Rate capability at current densities ranging from 0.2 to 2 A g^{-1}. (c-d) GCD profiles at different current densities corresponding to the rate capability.

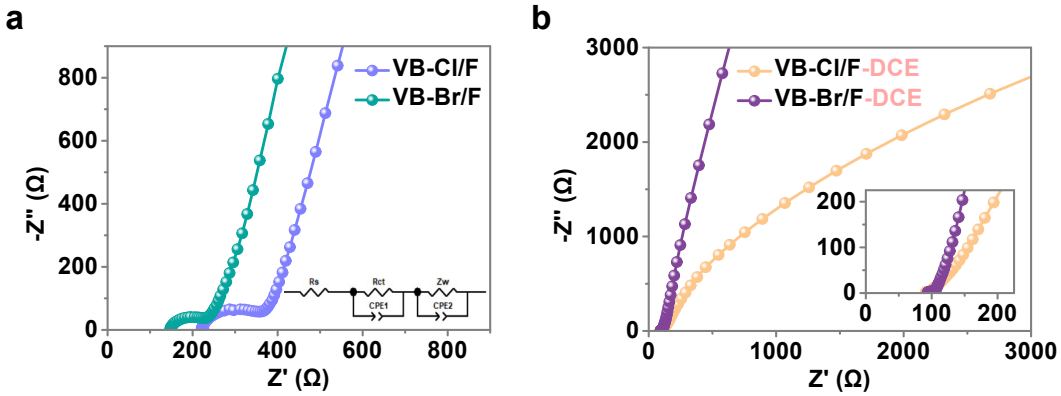

Fig. S17. EIS spectra of Zn||Te batteries at room temperatures in: (a) VB-Br/F and VB-Cl/F; (b) VB-Br/F-DCE and VB-Cl/F-DCE.

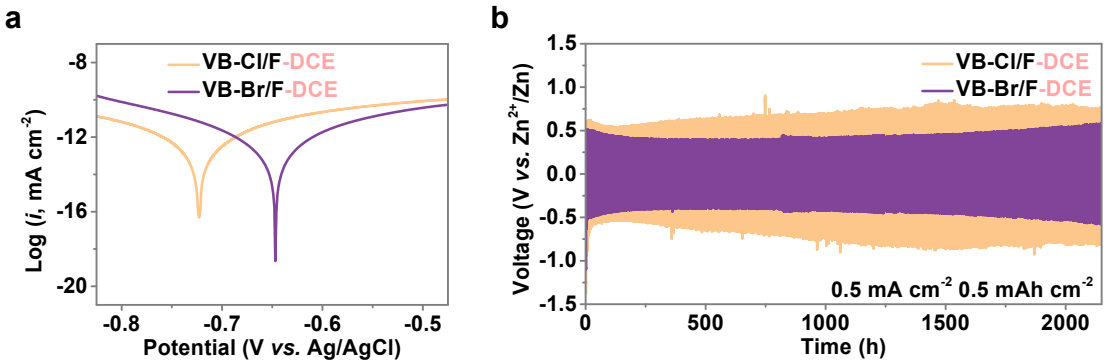

Fig. S18. (a) Tafel curves in a three-electrode system with VB-Br/F-DCE and VB-Cl/F-DCE. (b) Voltage-time curves of Zn||Zn symmetric cells at a current density and areal capacity of 0.5 mA cm^{-2} and 0.5 mA h cm^{-2}.

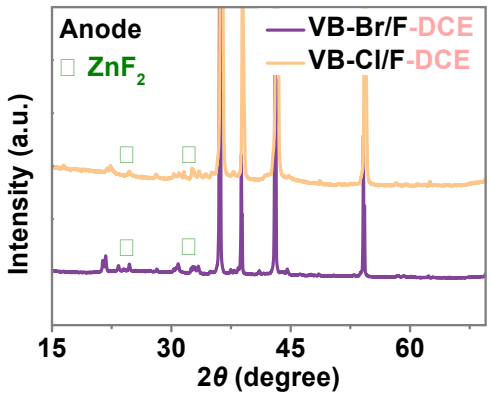

Fig. S19. XRD patterns of Zn cathodes in Zn||Te batteries at 1 A g^{-1} after 200 cycles in VB-Br/F-DCE and VB-Cl/F-DCE.

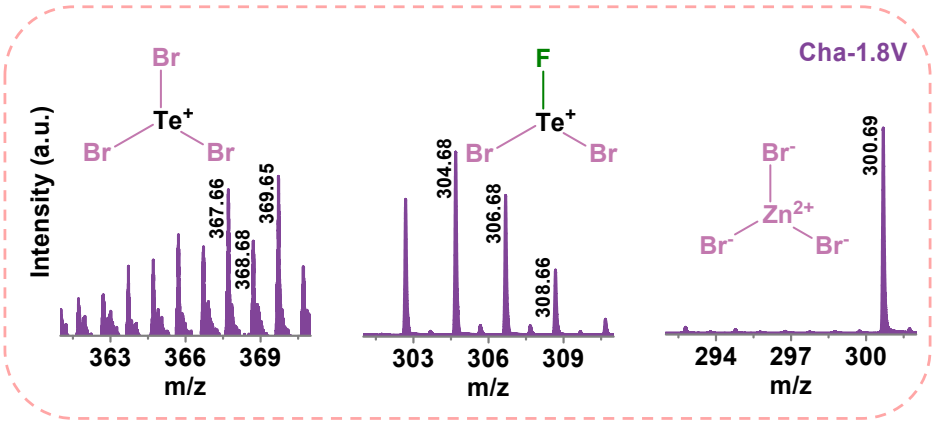

Fig. S20. The TOF-SIMS spectra of Te cathodes charged to 1.8 V (Cha-1.8V).

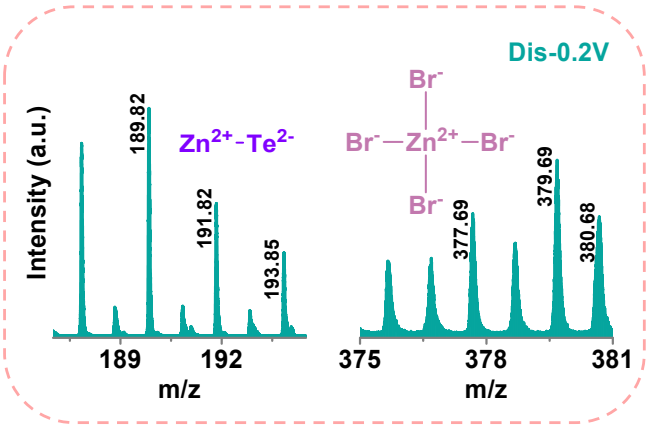

Fig. S21. The TOF-SIMS spectra of Te cathodes discharged to 0.2 V (Dis-0.2V).

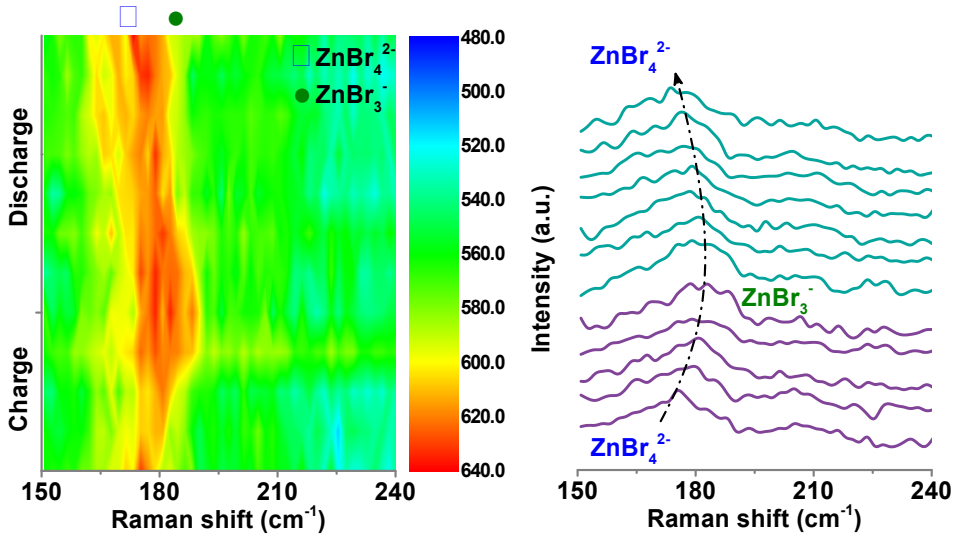

Fig. S22. *In-situ* Raman spectra of VB-Br/F-DCE at selected charge/discharge potentials.

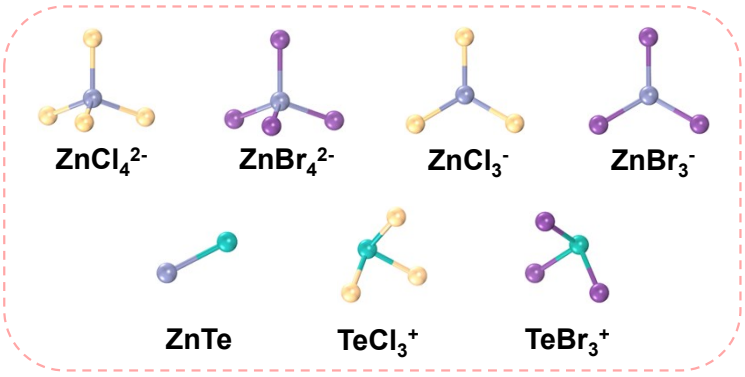

Fig. S23. The optimized theoretical structural models of ZnTe, $TeBr_3^+$, $TeCl_3^+$, $ZnBr_4^{2-}$, $ZnBr_3^-$, $ZnCl_4^{2-}$, and $ZnCl_3^-$.

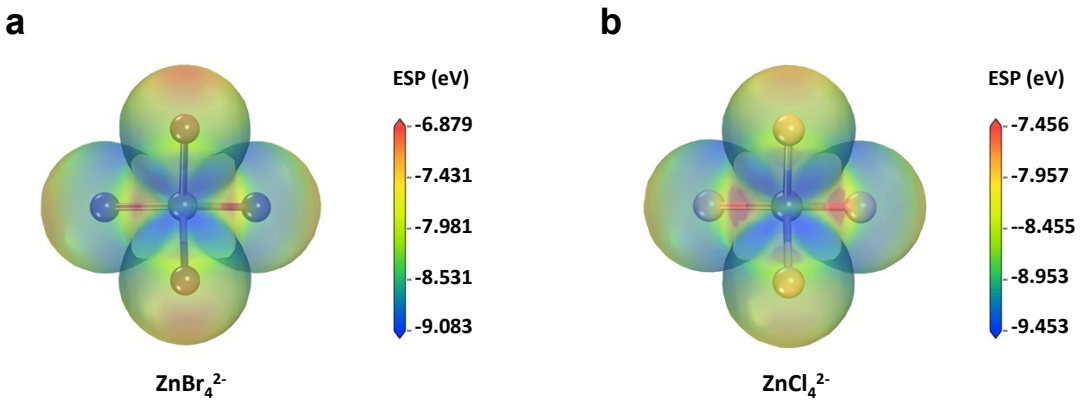

Fig. S24. ESP distribution of different active metal complex anions: (a) $ZnCl_4^{2-}$ and (b) $ZnBr_4^{2-}$.

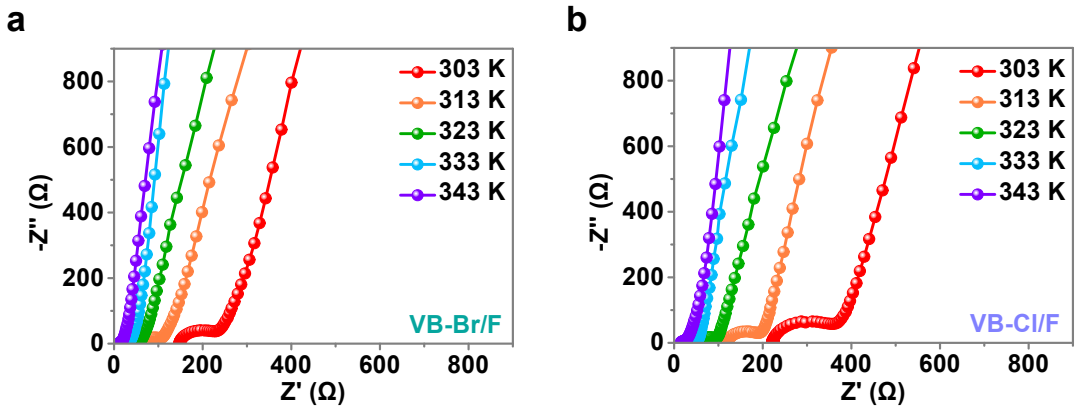

Fig. S25. Nyquist plots of Zn||Te batteries at different temperatures in: (a) VB-Br/F; and (b) VB-Cl/F.

4. Supplementary Tables

Table S1. Fitted R_{ct} of Te cathodes in different electrolytes at room temperature

Temperature (K)	VB-Br/F-DCE R_{ct} (Ω)	VB-Cl/F-DCE R_{ct} (Ω)	VB-Br/F R_{ct} (Ω)	VB-Cl/F R_{ct} (Ω)
303	13.6	28.1	125.6	184.9

Table S2. Gibbs free energy changes calculated by DFT for Te redox-amphoteric conversion and Zn plating/stripping in Zn‖Te batteries with VB-Br/F-DCE and VB-Cl/F-DCE.

Cathode ($ZnBr_4^{2-}$)	Δ_G (Hartree)	Δ_G (eV)	Anode ($ZnBr_4^{2-}$)	Δ_G (Hartree)	Δ_G (eV)
Te^0/Te^{2-}	0.260619	7.091808	Zn/Zn^{2+}	0.161430	4.392736
Te^{4+}/Te^0	0.667058	18.151582			
Cathode ($ZnCl_4^{2-}$)	Δ_G (Hartree)	Δ_G (eV)	Anode ($ZnCl_4^{2-}$)	Δ_G (Hartree)	Δ_G (eV)
Te^0/Te^{2-}	0.256735	6.986119	Zn/Zn^{2+}	0.157546	4.287047
Te^{4+}/Te^0	0.665073	18.09757			

Table S3. Fitted data of Te cathodes in VB-Br/F and VB-Cl/F at different temperatures.

Temperature (K)	VB-Br/F R_{ct} (Ω)	VB-Cl/F R_{ct} (Ω)
303	125.6	184.9
313	61.2	90.1
323	34.1	46.6
333	19.4	20.6
343	9.8	11.9

5. Supplementary References

1. T. Koketsu, C. Wu, Y. Huang and P. Strasser, *J. Appl. Electrochem.*, 2018, **48**, 1265-71.
2. J. Zheng, D. Wang, S. Kaushik, S. Zhang, T. Wada, J. Hwang, K. Matsumoto and R. Hagiwara, *EnergyChem*, 2022, **4**, 100075.
3. J. Feng, Y. Wang, Y. Xu, H. Ma, G. Wang, P. Ma and X. Yan, *Adv. Mater.* 2021, **33**, 2100887.
4. T. Lei, J. Pan, N. Wang, Z. Xia, Q. Zhang, J. Fan and L. Tao, *Mater. Horiz.* 2024, **11**, 1234.
5. Q. Fan, Y. Si, F. Zhu, W. Guo and Y. Fu, *Angew. Chem. Int.*, *Ed.*, 2023, **62**, e202306705.
6. X. Liu, A. Mariani, T. Diemant, M. E. D. Pietro, X. Dong, M. Kuenzel and A. Mele, S. Passerini, *Adv. Energy Mater.*, 2022, **12**, 2200862.
7. C. Lee, W. Yang and R. G. Parr, *Phys. Rev. B*, 1988, **37**, 785-89.
8. R. Ditchfield, W. J. Hehre and J. A. Pople, *J. Chem. Phys.*, 1971, **54**, 724-28.
9. H. Li, R. Meng, Y. Guo, B. Chen, Y. Jiao, C. Ye, Y. Long, A. Tadich, Q.-H. Yang, M. Jaroniec and S.-Z. Qiao, *Nat. Commun.*, 2021, **12**, 5714.
10. T. Lu and F. Chen, *J. Phys. Chem. A*, 2013, **117**, 3100-08.
11. T. Lu and F. Chen, *J. Comput. Chem.*, 2011, **33**, 580-92.
12. T. Lu and F. Chen, *Acta Phys. -Chim. Sin.*, 2011, **27**, 2786-92.